frontiers | Frontiers in Materials

TYPE Original Research
PUBLISHED 24 July 2025
DOI 10.3389/fmats.2025.1639947

OPEN ACCESS

EDITED BY
Yongtao Sun,
Tianjin University, China

REVIEWED BY
Yuzhou Du,
Xi'an University of Technology, China
Wenshu Yang,
Harbin Institute of Technology, China

*CORRESPONDENCE
Zheng Jia,
jz140@163.com

RECEIVED 03 June 2025
ACCEPTED 10 July 2025
PUBLISHED 24 July 2025

CITATION
Song T, Yang F, Niu X and Jia Z (2025) Mechanistic study on mechanical strengthening in As-extruded Mg-xSn (x = 0.5, 2, 4, 6 and 8 wt%) alloys.
Front. Mater. 12:1639947.
doi: 10.3389/fmats.2025.1639947

Mechanistic study on mechanical strengthening in As-extruded Mg-xSn (x = 0.5, 2, 4, 6 and 8 wt%) alloys

Tingting Song[1], Fu Yang[1], Xiaowei Niu[2] and Zheng Jia[1,2]*

[1]College of Mechanical Engineering, Shenyang University, Shenyang, China, [2]College of Environment, Liaoning Province Pollution Environmental Remediation Professional Technology Innovation Center and Shenyang Key Laboratory of Collaborative Technology Innovation for Industrial Pollution Reduction and Carbon Reduction, Shenyang University, Shenyang, China

This study systematically investigates the influence of Sn content (0.5–8 wt%) on the microstructural evolution and mechanical properties of as-extruded Mg-Sn alloys. By combining characterization techniques (XRD, scanning electron microscopy, EDS, and electron backscatter diffraction) with valence electron theory, the fundamental deformation mechanisms were elucidated. The results reveal that Sn content significantly modulates the distribution of Mg_2Sn phases, dynamic recrystallization behavior, and deformation modes. The increase of Sn content has no obvious effect on the grain size, but the area fraction of Mg_2Sn phase increases. The Mg-Sn bonds show the highest bonding energy among all possible atomic interactions, leading to enhanced mechanical properties. The alloy with 8% Sn demonstrates an optimal strength-ductility balance, due to grain refinement and strong texture effects. Furthermore, low-Sn alloys (≤2 wt%) deform primarily via basal slip, exhibiting ductile fracture characteristics, while high-Sn alloys (≥6 wt%) transition to a mixed fracture mode involving twinning and non-basal slip, attributed to increased Mg_2Sn phase content.

KEYWORDS

Mg-Sn alloy, Mg_2Sn phase, valence electron calculation, mechanical properties, fracture mechanism

1 Introduction

Magnesium alloys have demonstrated significant application potential in aerospace, transportation, and 3C products due to their exceptional specific strength, outstanding damping capacity, and excellent electrical conductivity (Zhu et al., 2012; Ma et al., 2024; Yang et al., 2024). However, inherent limitations such as insufficient absolute strength, poor corrosion resistance, and low ductility severely restrict their broader adoption. Under the current global trend of energy conservation and emission reduction, the development of magnesium alloys holds strategic importance.

Recent studies have shown that rare earth (RE) elements can significantly enhance the room- and high-temperature performance of magnesium alloys (Liu et al., 2018). However, their high cost hinders large-scale industrial applications. Consequently, the development of high-performance RE-free magnesium alloys has become a key research focus. Among these, the Mg-Sn system stands out as one of the most promising alternatives due to its unique high-temperature stability, notable solid-solution strengthening effect (Wei et al., 2008), and superior creep resistance (Shi et al., 2019; Shen et al., 2024), combined with

cost advantages. In the study of Mg-Sn alloys, the addition of Sn effectively refines the grain structure, transforming coarse columnar grains into fine equiaxed ones while forming short-rod-shaped Mg_2Sn strengthening phases, thereby significantly improving mechanical properties (Sun et al., 1999; Hu et al., 2024). The compressive creep resistance of Mg-7Sn alloy is comparable to that of the commercial AE42 alloy, and at 150°C, the performance of Mg-10Sn alloy even surpasses that of AE42. Nevertheless, this alloy system still suffers from grain coarsening tendencies, leading to considerable fluctuations in mechanical properties (Liu et al., 2007). Addressing this issue is critical to advancing the practical application of Mg-Sn-based alloys.

Currently, hot extrusion is the primary plastic forming method for wrought magnesium alloys. During the extrusion process, the alloy is subjected to intense triaxial compressive stresses, making this technique particularly suitable for processing low-ductility materials and maximizing the deformation potential of magnesium alloys. Additionally, extruded products exhibit high dimensional accuracy and excellent surface quality (Liu et al., 2024).

In recent years, first-principles calculations have become a vital tool in alloy research. However, their application to multi-component solid-solution systems still faces several critical challenges, particularly in selecting appropriate reference states (Chuanhao et al., 2025). To overcome these limitations, researchers have developed the self-consistent bond length difference (SCBLD) method (Lin et al., 2015; Lin et al., 2016), which significantly improves computational efficiency in determining the electronic structure of excited states in multicomponent alloys, thereby providing robust support for the valence electron (VE) theory framework (Liu and Lin, 2008; Zhang, 1990; Liu et al., 2002; Liu, 2002). Benefiting from the VE theory, researchers can efficiently obtain key physical parameters under excited states, including bond energy and interfacial energy. This advantage has led to substantial progress in studying alloy strengthening mechanisms, phase transformation processes, and atomic competitive behavior (Cui et al., 2024; Huang et al., 2023; Shixing et al., 2021; Zhang et al., 2017; Wang et al., 2008).

This study employs a multiscale research approach, integrating advanced experimental characterization techniques (including optical microscopy, transmission electron microscopy, and electron backscatter diffraction) with VE theoretical modeling to establish a comprehensive macro-to-micro investigation framework. Through this synergistic strategy, we systematically investigate the influence of Sn content on the microstructural evolution and mechanical properties of extruded Mg-Sn alloys. The research aims to develop novel Mg-Sn-based alloy materials with superior mechanical performance while providing a theoretical foundation for high-performance magnesium alloys.

2 Experimental methods

The Mg-xSn (x = 0.5, 2, 4, 6, 8) alloys were prepared using industrial pure Mg (99.9 wt%) and Sn (99.9 wt%). To eliminate internal stresses and minimize compositional segregation caused by non-equilibrium solidification, the as-cast ingots were subjected to homogenization treatment at 400°C for 12 h in a box-type resistance furnace, followed by water quenching. The homogenized ingots were then machined into cylindrical billets with dimensions of φ46 mm × 110 mm. Subsequently, the billets were processed via backward extrusion using a 600T four-column hydraulic press. The extrusion was conducted with a container temperature of 300°C, an extrusion speed of 1 mm/s, and an extrusion ratio of 14:1. Subsequently, the specimens machined from extruded rods were tested at room temperature using a Shimadzu AG-X (100 kN) electronic universal tensile testing machine, with a tensile speed of 1 mm/min. For each alloy, three repeated tensile tests were conducted, and the average values of these experimental data were calculated to obtain the final test results. Five alloy compositions were designed, and their actual chemical compositions were determined by inductively coupled plasma optical emission spectrometry (ICP-OES), as listed in Table 1.

TABLE 1 The actual chemical composition of the alloys.

Alloys	Actual chemical compositions (wt%)	
	Sn	Mg
Mg-0.5Sn	0.54	Bal
Mg-2Sn	2.31	Bal
Mg-4Sn	3.86	Bal
Mg-6Sn	5.85	Bal
Mg-8Sn	7.83	Bal

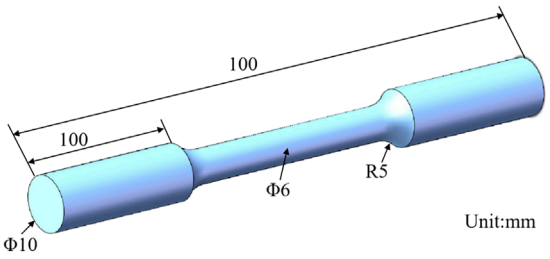

FIGURE 1
Dimensions of tensile specimens of the alloys at room temperature.

Phase identification of the alloys was performed using a Shimadzu-7000 X-ray diffractometer (XRD), with the acquired data analyzed by Jade 9 software through standard diffraction peak comparison to determine phase composition. Microstructural characterization was conducted using optical microscopy (OM), scanning electron microscopy (SEM), and electron backscatter diffraction (EBSD) after sample polishing and etching. The bond energy and interfacial energy of the alloys were calculated based on valence electron theory, as expressed by Equation 1 (Ren et al., 2025):

$$\overline{E}(hkl) = \frac{\Sigma \overline{E}_{\alpha}^{(hkl)} I_{\alpha}^{(hkl)}}{s^{(hkl)}} \quad (1)$$

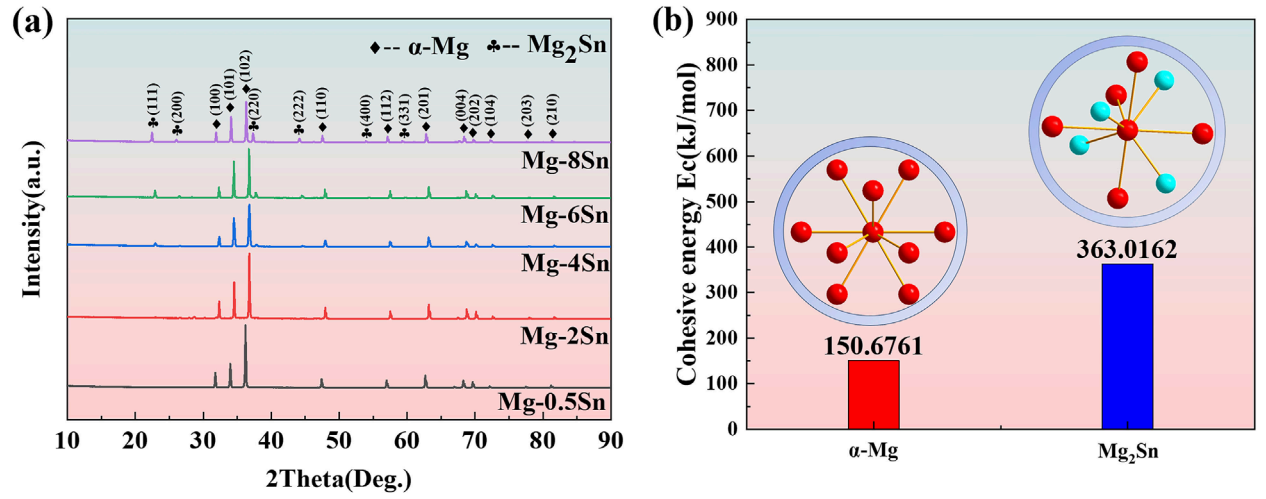

FIGURE 2
XRD patterns and binding energy diagram of the extruded alloy: **(a)** XRD patterns; **(b)** Binding energy.

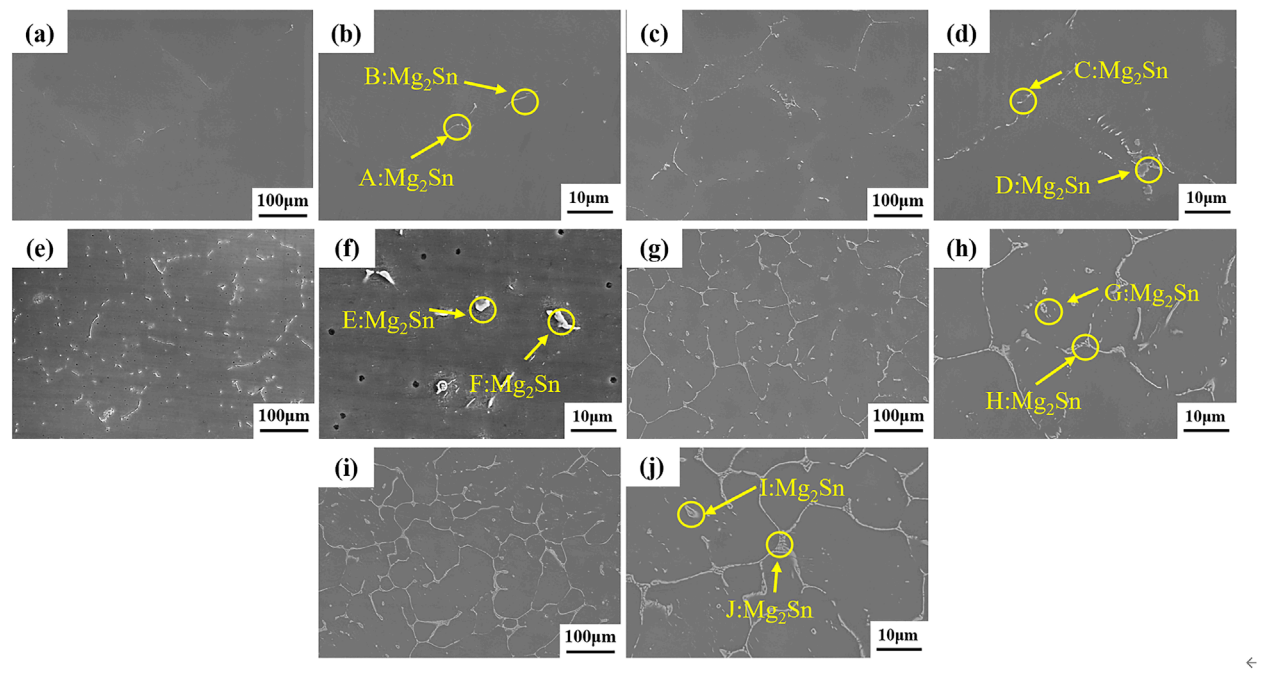

FIGURE 3
SEM morphology of the as-homogenized alloys: **(a, b)** Mg-0.5Sn, **(c, d)** Mg-2Sn, **(e, f)** Mg-4Sn, **(g, h)** Mg-6Sn, **(i, j)** Mg-8Sn.

The room-temperature tensile specimens were machined into tensile bars, as illustrated in Figure 1.

3 Experimental results

3.1 Microstructure

As shown in Figure 2a, XRD analysis indicates that when the Sn content is 0.5% and 2%, only weak diffraction peaks of the Mg_2Sn phases are present in the alloys. This is because the solid solubility exhibits significant temperature sensitivity, with the maximum solubility sharply decreasing from 14.85% at the eutectic point of 561.2°C to 0.45% at 200°C. During rapid cooling, due to the limited diffusion of solute elements, a substantial amount of Sn fails to complete the precipitation process and ultimately remains in a supersaturated solid solution within the solidified alloy matrix, without forming precipitates. When the Sn content exceeds 4%, a significant number of diffraction peaks of the Mg_2Sn phase can be detected in the XRD patterns, and their intensity markedly increases

TABLE 2 EDS analysis of precipitates in the as-homogenized alloys (at%).

Marked points	Chemical composition/at%		Phase composition
	Mg	Sn	
A	87.01	12.99	Mg_2Sn
B	81.34	18.66	Mg_2Sn
C	82.68	17.32	Mg_2Sn
D	81.25	18.75	Mg_2Sn
E	78.65	21.35	Mg_2Sn
F	78.66	21.24	Mg_2Sn
G	74.36	25.64	Mg_2Sn
H	77.82	22.18	Mg_2Sn
I	73.88	26.12	Mg_2Sn
J	70.05	29.95	Mg_2Sn

with higher Sn content. This phenomenon originates from solute segregation during solidification, which leads to Sn enrichment in local regions reaching the eutectic composition, thereby promoting the formation of the Mg_2Sn phase. With further increases in Sn content, the precipitation amount of this intermetallic compound shows a clear growth trend. Figure 2b displays the binding energies of α-Mg and Mg_2Sn phase clusters calculated using valence electron theory. The results reveal that the binding energy of the α-Mg matrix is much lower than that of the Mg_2Sn phase. This is because α-Mg contains only weak metallic bonds with delocalized electrons, resulting in low bond energy, which directly leads to the lower binding energy of the α-Mg matrix. In contrast, the Mg_2Sn phase exhibits both covalent and ionic bonds. From the perspective of bond energy analysis: on one hand, the sp^3 hybridization of Sn and the s-p orbitals of Mg form strong directional bonds; on the other hand, Sn acquires electrons from Mg, enhancing electrostatic attraction and thereby increasing the binding energy (Yuan et al., 2025). From a structural perspective: the unique cubic anti-fluorite structure of Mg_2Sn is denser than the hexagonal close-packed structure of Mg, with higher atomic coordination numbers, collectively enhancing stability (Fu et al., 2024).

To investigate the morphology and distribution characteristics of secondary phases in the alloys, both high-magnification and low-magnification SEM images were acquired, and the compositional analysis of secondary phases was performed using EDS spectroscopy. The homogenized Mg-Sn alloys primarily consisted of an α-Mg matrix with needle-like and network-shaped Mg_2Sn phases precipitated from the matrix, as shown in Figure 3 and Table 2. For the extruded alloys, the area fractions of phases were calculated using Image-Pro Plus software, with results presented in Figure 4 and Tables 3 and 4. The analytical results revealed that the Mg-Sn alloys were mainly composed of an α-Mg matrix and block-shaped/short rod-shaped Mg_2Sn phases. When the Sn content ranged from 0.5% to 4%, most secondary phases appeared fragmented and were distributed semi-continuously along the extrusion direction in a streamlined pattern within the matrix, exhibiting relatively uniform distribution with an average size of 0.85–0.97 μm. At 6% Sn content, the Mg_2Sn phases showed noticeable aggregation, being discretely distributed along grain boundaries as discontinuous lamellar eutectics while maintaining overall uniformity and fine characteristics. A small portion of secondary phases were crushed into gray-white lamellar structures aligned with extrusion bands during the extrusion process. When the Sn content reached 8%, the Mg_2Sn phases demonstrated increased aggregation and coarsening, forming semi-network structures at grain boundaries. During the high-temperature rapid backward extrusion process, the supersaturated Sn atoms in the homogenized alloy matrix underwent diffusion and redistribution, ultimately precipitating from the matrix in semi-network configurations.

Magnesium alloys undergoing hot extrusion plastic deformation develop deformation textures, whose presence significantly influences the mechanical properties of the alloys. Therefore, to further investigate the evolution of texture and grain orientation in the extruded alloys, EBSD technology was employed to analyze their microstructures. Figure 5 presents the grain orientation distribution maps and pole figures of the longitudinal sections of the alloys. The average grain sizes of the extruded alloys were determined through statistical calculations, as listed in Table 5. The alloy microstructures were homogeneous with relatively uniform grain sizes, predominantly exhibiting equiaxed morphology. Additionally, a small number of twins were observed in the microstructures of all five extruded alloys.

The (0001) basal texture distribution in the extruded rods primarily exhibits symmetry along the extrusion direction, with the $(11\bar{2}0)$ and $(10\bar{1}0)$ crystal planes showing more concentrated orientation distributions compared to the (0001) plane. As the Sn content increases, the macroscopic texture distribution of each crystal plane does not change significantly, but the texture intensity alters. Compared to the texture intensity of Mg-0.5Sn (7.35), those of Mg-2Sn, Mg-4Sn, Mg-8Sn and Mg-6Sn increase to 7.39, 7.62, 12.73 and 12.81, respectively. This indicates that increasing Sn content enhances the texture intensity.

To investigate the influence mechanisms of grain boundary angles and twin boundaries on mechanical properties, we systematically analyzed the misorientation angle distributions of all five alloys, as shown in Figure 6. The results demonstrate that all five alloys exhibit similar distribution trends, primarily consisting of a large proportion of low-angle grain boundaries (LAGBs, 2°–15°) and a small fraction of high-angle grain boundaries (HAGBs, ≥15°). This phenomenon can be attributed to the continuous increase in strain leading to intensified intragranular deformation, which significantly elevates the intragranular orientation gradient and consequently promotes the formation of HAGBs. Twin boundary characterization reveals that when defining boundaries with misorientation angles of 86° ± 5° as twin boundaries according to crystallographic standards, all five alloys display distinct characteristic peaks at ~86°. This finding confirms that substantial twinning deformation occurred during the deformation process, forming typical twin structures in all alloys. From the distribution perspective, LAGBs dominate in all five alloys, which aligns with the evolutionary pattern of

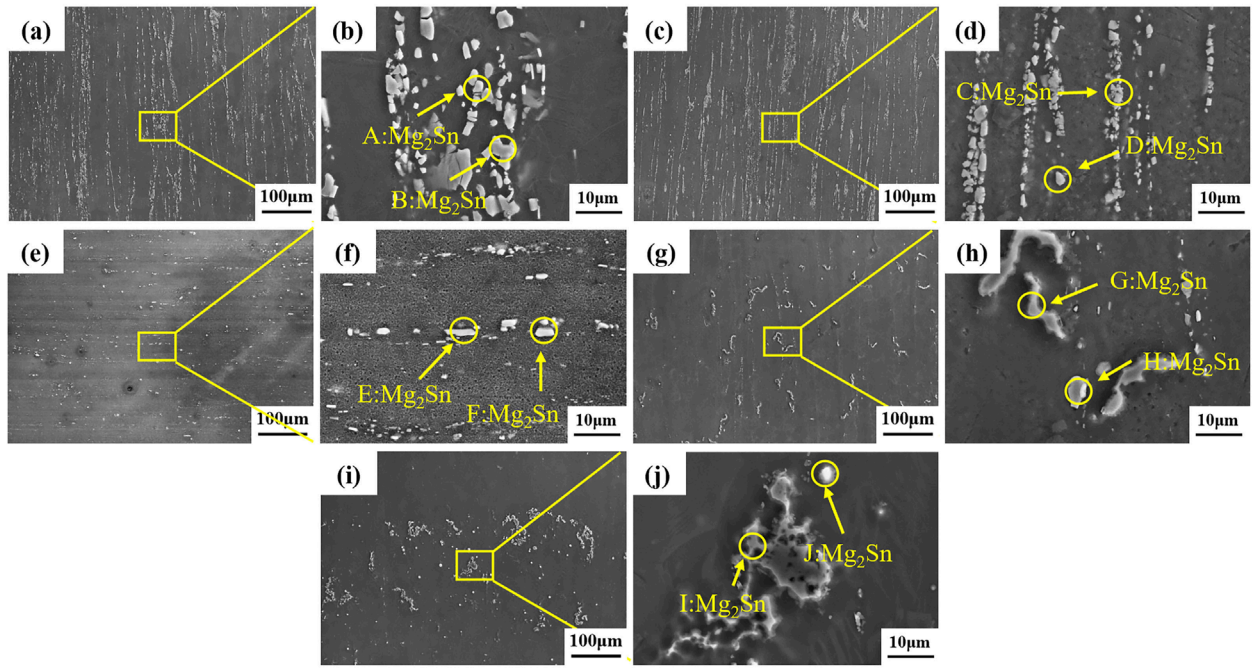

FIGURE 4
SEM image of the as-extruded alloys: **(a, b)** Mg-0.5Sn; **(c, d)** Mg-2Sn; **(e, f)** Mg-4Sn; **(g, h)** Mg-6Sn; **(i, j)** Mg-8Sn.

TABLE 3 EDS analysis of the as-extruded alloys (at%).

Marked points	Chemical composition/at%		Phase composition
	Mg	Sn	
A	84.05	15.95	Mg_2Sn
B	70.33	29.67	Mg_2Sn
C	82.55	17.45	Mg_2Sn
D	83.07	13.93	Mg_2Sn
E	69.93	30.07	Mg_2Sn
F	82.23	17.77	Mg_2Sn
G	84.24	15.76	Mg_2Sn
H	79.32	20.68	Mg_2Sn
I	85.01	14.99	Mg_2Sn
J	62.31	37.69	Mg_2Sn

TABLE 4 Average size and area fraction of the second phase in the as-extruded alloys.

Alloy	Area fraction of second phase (%)	The average size of the second phase (μm)
Mg-0.5Sn	4.6 ± 1.2	0.85
Mg-2Sn	7.1 ± 1.5	0.93
Mg-4Sn	10.9 ± 1.1	0.97
Mg-6Sn	14.7 ± 1.2	0.99
Mg-8Sn	17.5 ± 0.8	1.13

grain refinement and increasing orientation gradients during plastic deformation. Simultaneously, the presence of characteristic peaks at ~86° further indicates that twinning deformation plays a significant role in the plastic deformation process.

Figure 7 presents the recrystallization microstructure distribution characteristics of extruded Mg-xSn alloys with varying Sn contents (x = 0.5, 2, 4, 6, 8 wt%). Through electron backscatter diffraction (EBSD) analysis, the microstructures were systematically differentiated into dynamically recrystallized grains (blue), sub-grains (yellow), and deformed grains (red) using color coding, revealing the influence of Sn content on dynamic recrystallization behavior. The results demonstrate that as Sn content increases, the volume fraction of dynamically recrystallized grains exhibits a nonlinear trend of initial decrease followed by increase, while the distributions of subgrains and deformed grains show opposite evolutionary characteristics. This microstructural evolution originates from the dynamic equilibrium mechanism between stored energy release and interface reorganization: deformed grains, as initial high-energy-state structures, gradually evolve into sub-grains through dislocation rearrangement, ultimately

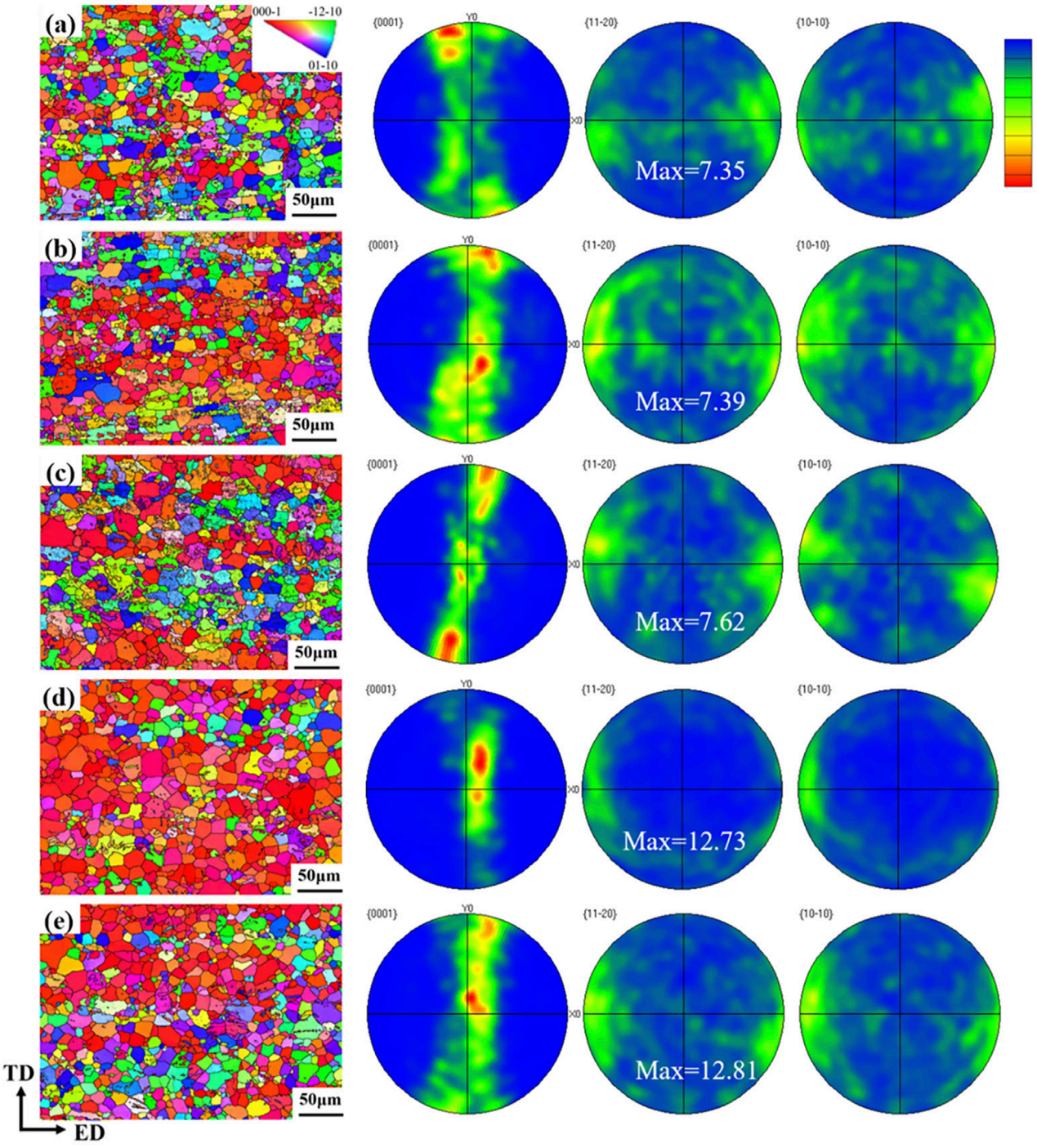

FIGURE 5
IPF diagram and PF diagram of the as-extruded experimental alloys: **(a)** Mg-0.5Sn; **(b)** Mg-2Sn; **(c)** Mg-4Sn; **(d)** Mg-6Sn; **(e)** Mg-8Sn.

transforming into dynamically recrystallized grains under appropriate thermodynamic conditions to achieve microstructural homogenization. Notably, when Sn content falls within the 2–4 wt% range, the alloys display pronounced recrystallization suppression, likely attributable to the drag effect of Sn solute atoms on grain boundary migration. However, when Sn content increases to 6–8 wt%, the recrystallization degree significantly improves, suggesting that higher Sn concentrations may promote recrystallization by altering stacking fault energy or dislocation motion modes.

The Schmid factor (SF), as a critical parameter characterizing the activation difficulty of crystal slip systems, quantitatively reflects the resolved shear stress efficiency of specific slip systems under applied stress (Zhang et al., 2014). In this study, EBSD

TABLE 5 Grain size of as-extruded alloy.

Alloys	Grain size/μm
Mg-0.5Sn	21
Mg-2Sn	20
Mg-4Sn	15
Mg-6Sn	22
Mg-8Sn	19

technology was systematically employed to determine the SF distributions of basal <a>, prismatic <c>, and pyramidal <c+a> slip systems during tensile deformation along the extrusion direction in Mg-xSn (x = 0.5–8 wt%) alloys, revealing the influence of Sn content on deformation mechanisms, as illustrated in Figure 8. Under room-temperature deformation conditions, magnesium alloys exhibit significant differences in critical resolved shear stress (CRSS) among various slip systems: basal slip possesses the lowest CRSS and, combined with its high slip plane density, serves as the primary carrier of plastic deformation (Zhai et al., 2024). Meanwhile, twinning deformation, as another important deformation mechanism with relatively low activation stress (2–3 MPa), provides additional strain accommodation paths (Li et al., 2024). Experimental results demonstrate that as Sn content increases from 0.5 wt% to 8 wt%, the basal SF value monotonically decreases from 0.221 to 0.181, while the prismatic SF increases from 0.434 to 0.449, and the pyramidal SF remains stable within 0.389–0.409. This trend indicates that Sn alloying significantly alters the orientation characteristics of magnesium alloys, specifically manifested as: the geometric softening effect of basal slip continuously weakens with increasing Sn content, while the potential deformation capacity of non-basal slip systems gradually enhances. Detailed analysis of the deformation mechanism transition reveals that when basal SF values drop below 0.2 (Mg-4Sn to Mg-8Sn alloys), the activation difficulty of basal slip significantly increases. This phenomenon primarily originates from the elevated CRSS caused by the pinning effect of Sn solute atoms on basal dislocations. Notably, although prismatic and pyramidal slips exhibit higher SF values (>0.43), their actual contributions at room temperature remain limited due to the intrinsically high CRSS characteristics of non-basal slips in HCP structures. Under these circumstances, {1,012}<1011> tensile twinning (SF ≈ 0.49), with its lower activation stress, likely becomes the dominant mechanism for accommodating c-axis strain, a conclusion that aligns well with previous reports on Sn-induced twinning promotion (Zhou, 2024). In low-Sn-content alloys (Mg-0.5Sn), the basal SF value of 0.221 approaches the typical activation threshold for basal slip in HCP metals (SF ≈ 0.2), indicating basal slip remains the primary deformation mode. However, with increasing Sn content, the synergistic effect between decreasing basal SF and increasing non-basal SF values ultimately leads to a transition in deformation mechanisms from basal-slip-dominant to a coordinated combination of twinning and non-basal slip. In summary, Mg-Sn alloys exhibit pronounced composition-dependent deformation mechanisms: basal slip dominates at low Sn contents (≤2 wt%), while a coordinated deformation mode combining twinning and non-basal slip emerges at high Sn contents (≥6 wt%).

3.2 Tensile properties

Figure 9 presents the engineering stress-strain curves of five extruded Mg-Sn alloy rods, with their mechanical properties summarized in Table 6. The results demonstrate that all alloys exhibit considerable ductility, with elongation values exceeding 14%. As Sn content increases, the elongation shows an inverted N-shaped trend of initial decrease, subsequent increase, and final reduction, with Mg-4Sn alloy achieving the maximum elongation (17.5%). Microstructural analysis suggests this enhanced ductility likely correlates with its relatively high proportion of low-angle grain boundaries (LAGBs) and degree of dynamic recrystallization (DRX). Regarding strength characteristics, increasing Sn content improves mechanical performance. When Sn content reaches 8 wt%, the Mg-8Sn alloy demonstrates optimal strength properties, with yield strength (YS) and ultimate tensile strength (UTS) reaching 236 MPa and 144 MPa, respectively. Compared to the low-Sn-content Mg-0.5Sn alloy, the Mg-8Sn alloy shows remarkable strength enhancement. Microstructural comparison reveals that the Mg-8Sn alloy possesses finer grain size and higher pole density in its deformation texture. Therefore, we conclude that the superior strength of Mg-8Sn alloy primarily results from the combined effects of grain refinement strengthening and texture strengthening.

Through correlative analysis of fracture morphology and mechanical properties in Mg-Sn alloys, this study reveals the intrinsic relationship between fracture mechanisms and microstructural evolution. Fractographic analysis demonstrates composition-dependent fracture characteristics. As observed in Figure 10 SEM images, low-Sn-content alloys (Mg-0.5Sn) exhibit typical ductile fracture features characterized by dimples with non-uniform sizes. Combined with EDS results in Table 7, the second-phase particles in Mg-4Sn alloy dimples are identified as Mg_2Sn phase. This observation aligns with the mechanical properties (Rm = 206 MPa, ε = 16.8%), indicating a fracture process involving: initial interfacial decohesion between second-phase particles and matrix forming microvoids, subsequent void growth during plastic deformation, and final fracture through void coalescence. When Sn content increases to 2 wt% (Mg-2Sn), the alloy demonstrates improved tensile strength (221 MPa) with 14.3% elongation. The fracture surface maintains ductile characteristics but shows more uniform dimple size distribution, reflecting improved Mg_2Sn phase dispersion. This microstructural feature enables simultaneous strength enhancement and preserved ductility. Notably, Mg-4Sn alloy exhibits optimal strength-ductility balance (Rm = 227 MPa, ε = 17.5%). Its fracture surface displays homogeneous fine dimples, suggesting that approximately 4 wt% Mg_2Sn phase effectively promotes dislocation accumulation for strengthening without significantly compromising plasticity. This synergy likely relates to optimized dynamic recrystallization. With further Sn increase to 6-8 wt% (Mg-6Sn and Mg-8Sn), while tensile strengths reach 232 and

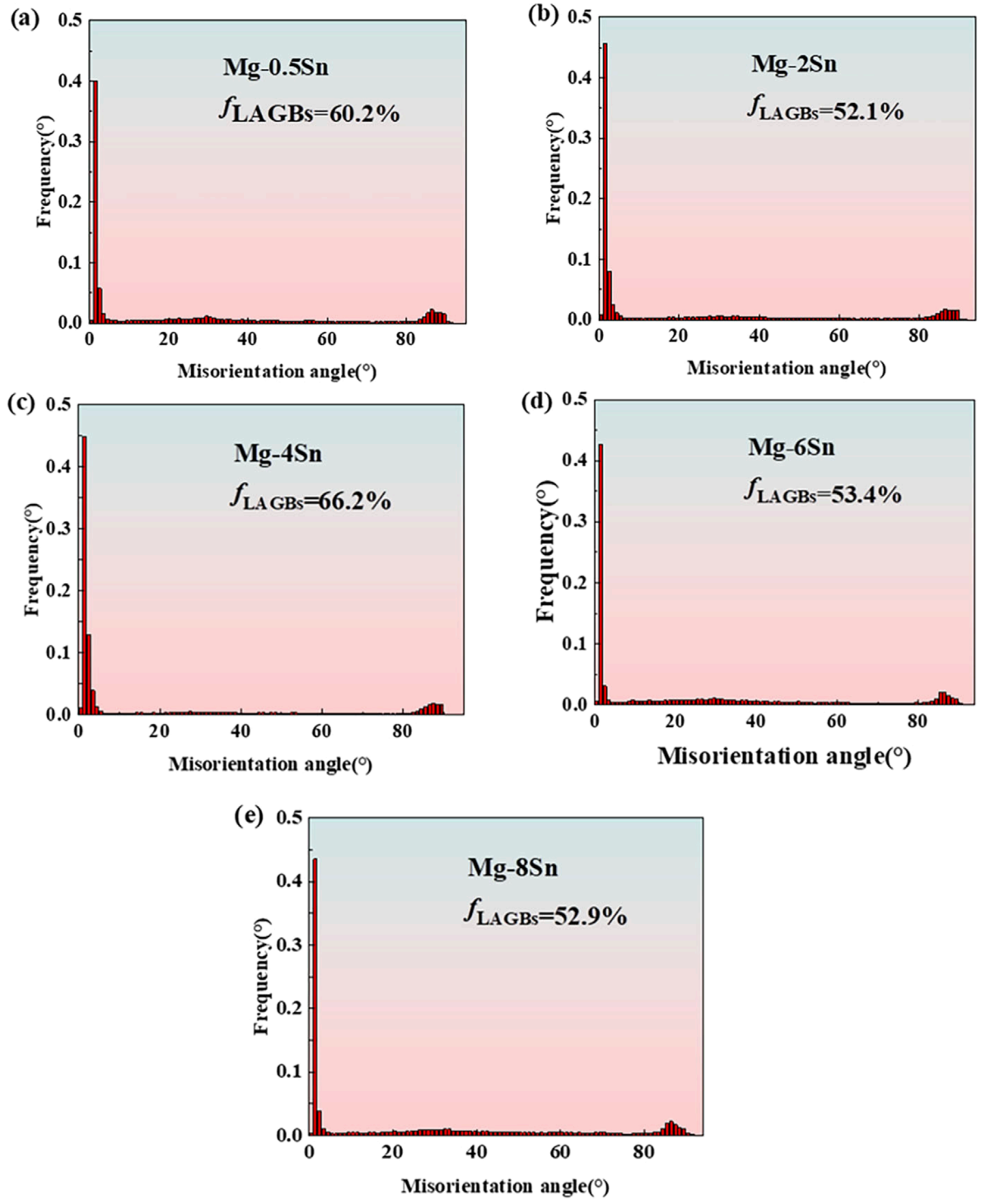

FIGURE 6
Distribution map of orientation angle of the as-extruded experimental alloys: **(a)** Mg-0.5Sn; **(b)** Mg-2Sn; **(c)** Mg-4Sn; **(d)** Mg-6Sn; **(e)** Mg-8Sn.

236 MPa respectively, elongations stabilize around 16%. The fracture morphology shows transitional characteristics: retained dimple structures coexist with cleavage features, forming typical mixed-mode fracture. This transition indicates gradual evolution from purely ductile to quasi-cleavage fracture with increasing Mg_2Sn content. Particularly in Mg-8Sn alloy, fine DRX grains and strong deformation texture contribute to excellent strength, while excessive second phases enhance local embrittlement tendency.

From the perspective of microstructural evolution during fracture: low-Sn alloys (0.5–2 wt%) primarily rely on dislocation slip and interfacial decohesion to accommodate deformation; medium-Sn alloys (4 wt%)

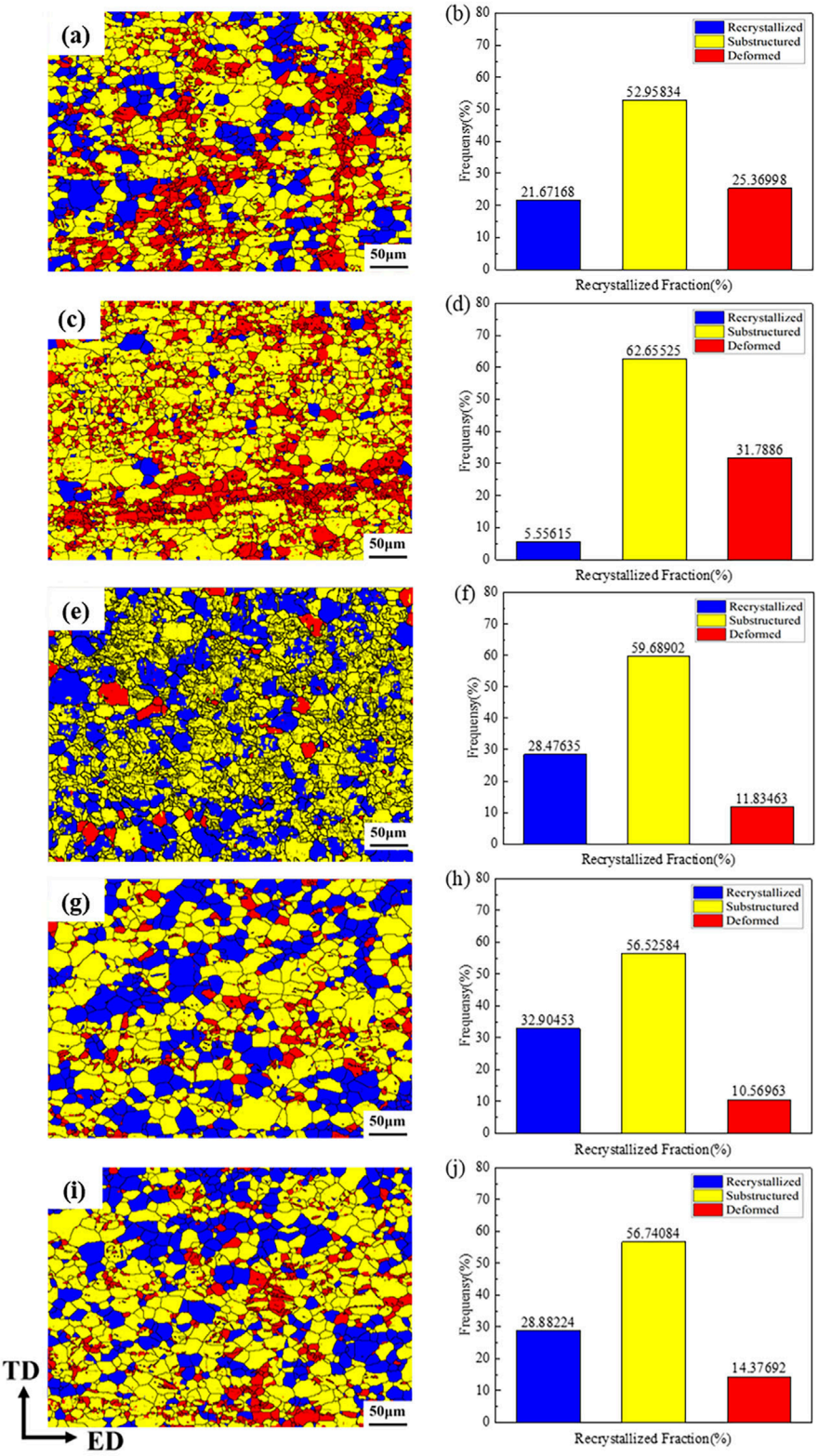

FIGURE 7
Recrystallisation distribution of the as-extruded alloys: **(a, b)** Mg-0.5Sn; **(c, d)** Mg-2Sn; **(e, f)** Mg-4Sn; **(g, h)** Mg-6Sn; **(i, j)** Mg-8Sn.

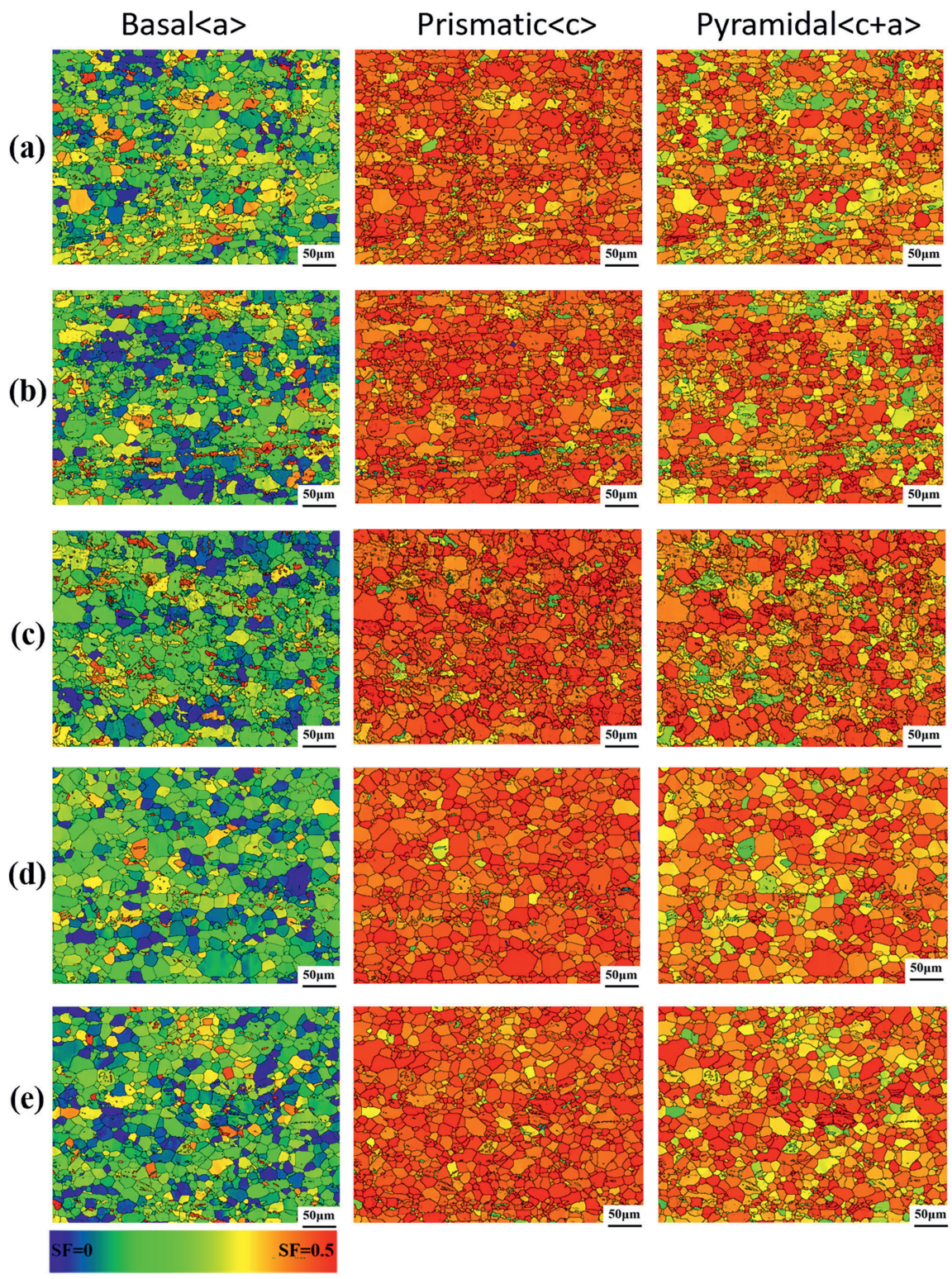

FIGURE 8
(Continued).

achieve strength-ductility synergy through optimized DRX degree and second-phase distribution; while high-Sn alloys (6–8 wt%), despite exhibiting easier crack propagation along phase boundaries due to abundant Mg_2Sn phases, still maintain certain plasticity through grain refinement strengthening effects.

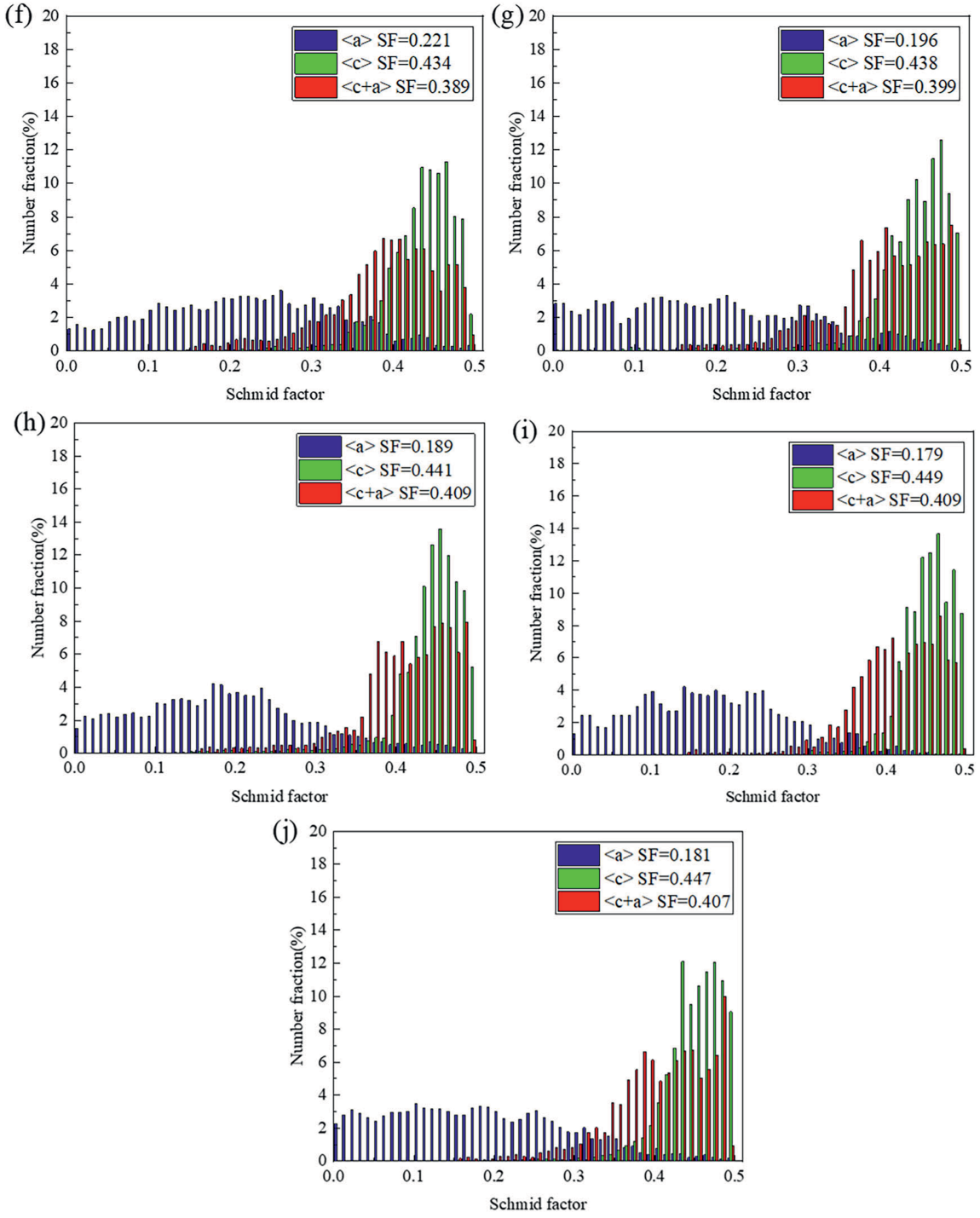

FIGURE 8
(Continued). Schmid factor distribution of the as-extruded alloys: **(a, b)** Mg-0.5Sn; **(c, d)** Mg-2Sn; **(e, f)** Mg-4Sn; **(g, h)** Mg-6Sn; **(i, j)** Mg-8Sn.

4 Discussion

The α-Mg matrix exhibits a typical hexagonal close-packed (HCP) structure, as shown in Figure 11a, with its primary slip plane being the basal plane. Simultaneously, the basal plane possesses the highest interfacial energy of 18821.87029 KJ/(nm^2·mol), as illustrated in Figure 11b. The Mg_2Sn phase, serving as a crucial strengthening phase in Mg-Sn alloys, significantly influences the mechanical properties through its anti-fluorite type face-centered cubic (FCC) structure. In this structure, cations (Mg^{2+}) form the FCC lattice framework while anions (Sn^{2-}) occupy tetrahedral interstitial sites, resulting in a unit cell arrangement where 4 Sn atoms are located at FCC nodes and 8 Mg atoms fill the interstitial positions, as depicted in Figure 11c. Table 8 presents

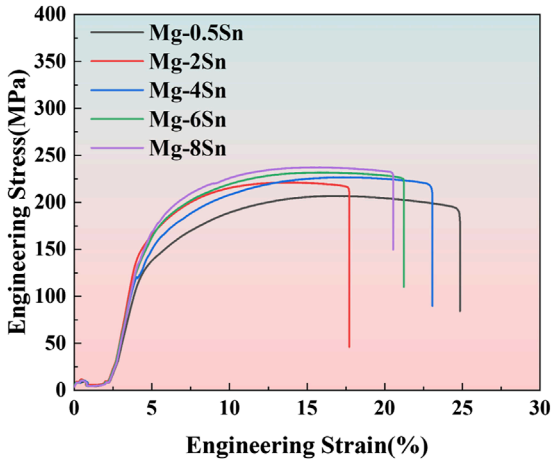

FIGURE 9
Stress-strain curves of the as-extruded alloys at room temperature.

TABLE 6 Room temperature mechanical properties of the as-extruded alloys.

Alloys	R_m/MPa	$R_{p0.2}$/MPa	ε %
Mg-0.5Sn	206 ± 0.4	134 ± 3.4	16.8 ± 0.7
Mg-2Sn	221 ± 1.6	147 ± 1.5	14.3 ± 0.3
Mg-4Sn	227 ± 1.6	144 ± 2.1	17.5 ± 0.7
Mg-6Sn	232 ± 0.8	149 ± 1.6	16.6 ± 0.6
Mg-8Sn	236 ± 0.5	144 ± 1.3	16.3 ± 0.3

the valence electron structure (VES) parameters and covalent bond energies of Mg_2Sn. Analysis of bond energy distribution, as shown in Figures 11d, e, reveals that the Mg-Sn bonds possess the strongest bond energy. These strong bonds require higher energy for fracture during deformation, endowing the Mg_2Sn phase with superior structural stability and rigidity. In contrast, the B-type Sn-Sn bonds exhibit the weakest bond energy, potentially serving as vulnerable points during deformation. During plastic deformation, the strong Mg-Sn bonds significantly impede dislocation slip (since phase transformation only occurs when the strongest bonds break, the strongest bonds are primarily considered). Consequently, dislocation motion must initiate bond breaking at interfaces where strong bonds are distributed, as this requires the minimum driving force for destruction. The interface with the highest interfacial energy is therefore selected, where the distribution of strong bonds leads to elevated interfacial energy. The potential barrier that dislocations must overcome when moving parallel to this Mg_2Sn unit cell interface is substantially higher than those for the α-Mg basal plane and Mg_2Sn (0 $\bar{1}$ 0) crystal plane, thereby enhancing the alloy's yield strength. However, the presence of weak Sn-Sn bonds may lead to local stress concentration, becoming preferred sites for dislocation nucleation. This heterogeneity in bond energy distribution directly affects dislocation motion and interfacial behavior, consequently regulating the alloy's deformation mechanism. The calculations demonstrate that:

The Mg_2Sn (1 $\bar{1}$ 0) crystal plane exhibits extremely high interfacial energy (3959.76726 kJ/(nm^2·mol)), indicating that dislocation slip is difficult to occur on this plane, which tends to release energy through cleavage fracture. In contrast, the (0 $\bar{1}$ 0) crystal plane shows extremely low interfacial energy (≈7.6041 × 10^{-12} kJ/(nm^2·mol)), potentially serving as an easy slip channel for dislocations and promoting local plastic deformation. This non-uniform distribution of interfacial energy leads to dislocation pile-up at high-energy interfaces during deformation. Specifically, high interfacial energy planes hinder dislocation slip, while low interfacial energy planes preferentially facilitate dislocation propagation. The inconsistency between these two effects exacerbates the non-uniformity of dislocation motion across slip systems in the alloy. Combining with the binding energy distribution shown in Figure 2b, the Mg_2Sn clusters possess high binding energy, meaning any transformation must involve breaking the strongest bonds, requiring atomic movement along the (1 $\bar{1}$ 0) crystal plane. However, dislocations preferentially select the plane with the lowest interfacial energy for motion, making it difficult to break the strongest bonds. Consequently, the strengthening phase remains highly stable, thereby enhancing the material's strength. From the perspective of dislocation-crystal cell interaction, the strengthening effect of Mg_2Sn phase primarily originates from the pinning of dislocations by strong bonding interactions. However, weak bonds and interfacial energy differences also introduce potential failure risks. Specifically, while dislocations slip along low-energy interfaces, they accumulate at high-energy interfaces. The resulting local stress concentration at high-energy interfaces may lead to microcrack propagation along high-energy crystal planes (1 $\bar{1}$ 0), thereby reducing fracture toughness.

The strengthening mechanisms of Mg-Sn alloys are primarily attributed to grain refinement, texture strengthening, and precipitation strengthening. Calculate the proportions of the three strengthening mechanisms using Equations 2–4. The strengthening effect of grain boundaries in the as-extruded alloy was calculated using the Hall-Petch equation (Hall, 1951; Petch, 1953):

$$\sigma_{GB} = \sigma_0 + K_y d^{-1/2} \tag{2}$$

Where "σ_{GB}" is the contribution of grain boundary strengthening to yield strength, "σ_0" is the lattice friction stress, "k_y" is the strengthening coefficient, and "d" is the grain size. For a given alloy system, "σ_0" and "k_y" are constants. For Mg-Sn alloys, the parameters of pure magnesium can be used as approximations: σ_0 = 11 MPa and k_y = 220 MPa μm$^{-1/2}$ (Zhu et al., 2021; Saba et al., 2019).

The Mg_2Sn phase is a brittle phase with high hardness. When dislocations glide past Mg_2Sn particles, they bypass the particles through the Orowan mechanism, leading to dislocation accumulation near the precipitates and resulting in strengthening. The contribution of precipitation strengthening to the yield strength was calculated using the Orowan mechanism (Ma et al., 2014; Wang et al., 2020):

$$\Delta\sigma_{Oroowan} = M\frac{Gb}{2\pi\sqrt{1-\nu}}\frac{1}{dp\left(\sqrt{\frac{\pi}{4f}}-1\right)}ln\frac{dp}{b} \tag{3}$$

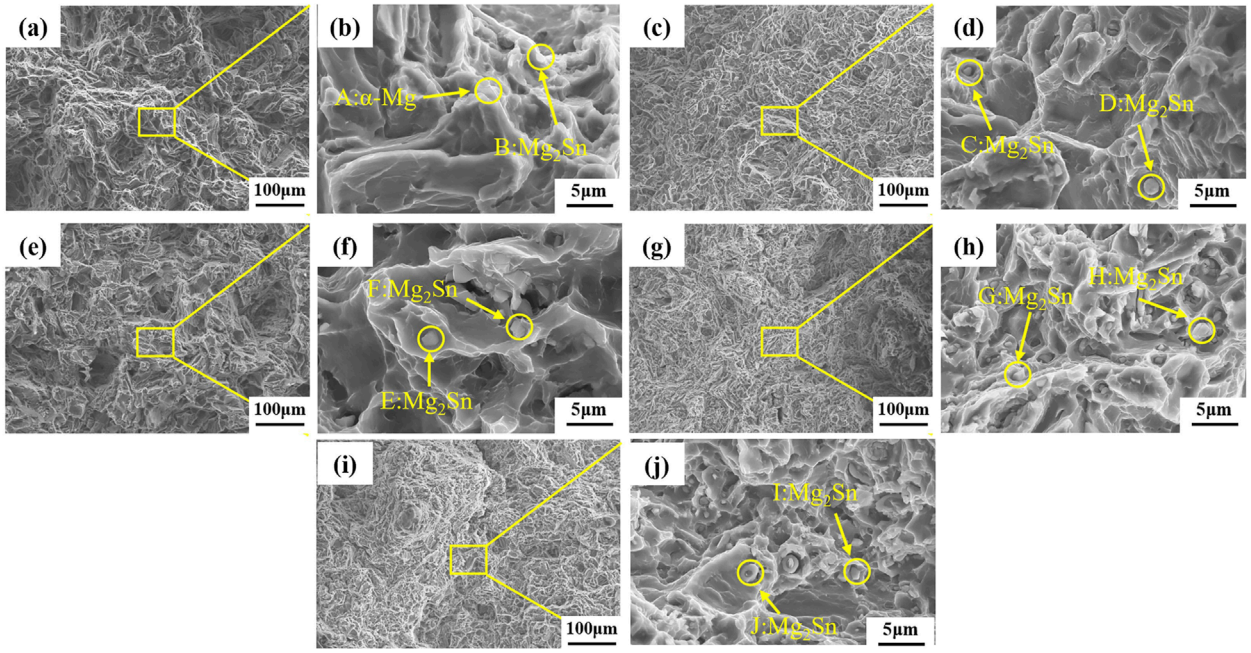

FIGURE 10
SEM morphology of fracture cross section of as-extruded alloy **(a, b)** Mg-0.5Sn; **(c, d)** Mg-2Sn; **(e, f)** Mg-4Sn; **(g, h)** Mg-6Sn; **(i, j)** Mg-8Sn.

TABLE 7 EDS of precipitated phases on the fracture surface of the as-extruded alloys (at%).

Marked points	Chemical composition/at%		Phase composition
	Mg	Sn	
A	99.76	0.24	α-Mg
B	87.34	12.66	Mg_2Sn
C	87.02	12.98	Mg_2Sn
D	88.64	11.36	Mg_2Sn
E	85.12	14.88	Mg_2Sn
F	80.29	19.71	Mg_2Sn
G	77.43	22.57	Mg_2Sn
H	84.57	15.43	Mg_2Sn
I	83.68	16.32	Mg_2Sn
J	80.43	19.57	Mg_2Sn

Where "$\Delta\sigma_{Orowan}$" is the strengthening contribution of precipitates to yield strength; "M" is the average Taylor factor (approximately 4.5); "G" is the shear modulus (1.66 × 104 MPa) (Kang et al., 2017); "b" is the Burgers vector (3.21×10^{-10} m) (Kang et al., 2017); "ν" is Poisson's ratio (0.35) (Yang et al., 2007); "dp" is the average size of precipitates; and "f" is the volume fraction of precipitates.

The contribution of texture strengthening to the yield strength of the alloy can be described by the following equation (Yin et al., 2017; Yakubtsov et al., 2008):

$$\sigma_{texture} = m\tau_0 \tag{4}$$

Where "m" is the Taylor orientation factor related to texture strength (approximately 6.5 times the texture strength of the alloy), and "τ_0" is the CRSS of basal slip (approximately 0.49 MPa) (Bu et al., 2015).

Using the above equations, the individual contributions of grain boundaries, second-phase precipitates, and texture to the strength were calculated, as shown in Table 9.

5 Conclusion

1. With increasing Sn content (0.5–8 wt%), the microstructure of extruded Mg-Sn alloys exhibits systematic evolution: The Mg_2Sn phase transitions from finely dispersed particles to coarsened semi-network structures, while the dynamic recrystallization (DRX) degree initially decreases and subsequently increases. This microstructural evolution directly influences the mechanical properties, where the Mg-8Sn alloy demonstrates the optimal strength-ductility balance (ultimate tensile strength: 236 MPa, elongation: 16.3%), whereas the Mg-8Sn alloy achieves the highest strength (ultimate tensile strength: 236 MPa) through grain refinement and texture strengthening.

10.3389/fmats.2025.1639947

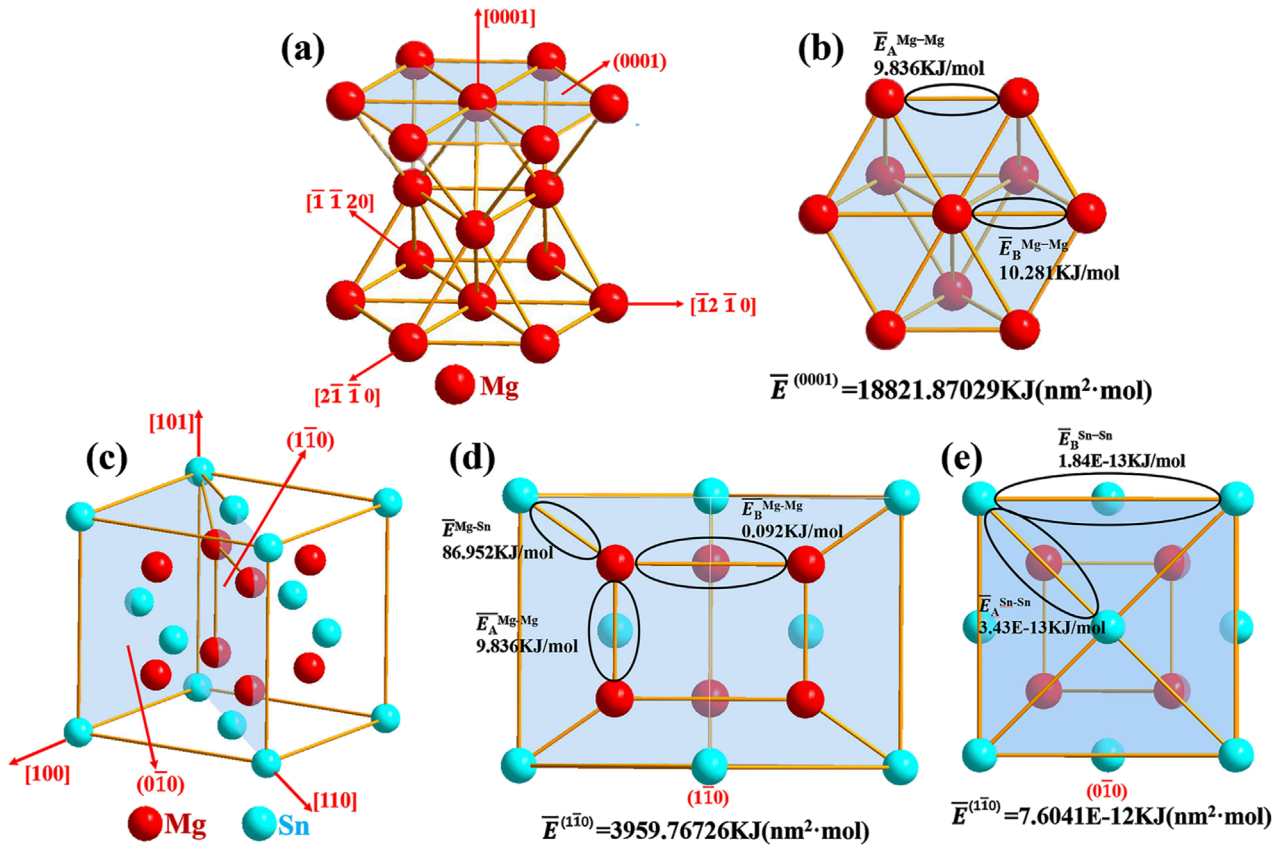

FIGURE 11
Analysis of bond energy at Mg_2Sn phase interfaces: **(a)** α-Mg basal plane; **(b)** α-Mg (0001) crystal plane; **(c)** Two typical crystal planes of Mg_2Sn; **(d)** Mg_2Sn (1 $\bar{1}$ 0) crystal plane; **(e)** Mg_2Sn (0 $\bar{1}$ 0) β crystal plane.

TABLE 8 Valence electron structure (VES) parameters and covalent bond energy of Mg_2Sn.

Phase	CBN	EBN	EBL (nm)	SEPN	BE (KJ/mol)
α-Mg	$\overline{E}_A^{Mg-Mg}$	6	0.32042	0.1056167	9.83642
	$\overline{E}_B^{Mg-Mg}$	6	0.31918	0.1099716	10.2813
Mg_2Sn	$\overline{E}_A^{Mg-Mg}$	4	0.32041	0.10561	9.83631
	$\overline{E}_B^{Mg-Mg}$	8	0.45204	1.39117E-03	9.18371E-02
	$\overline{E}^{Mg-Sn}$	5.3	0.29295	0.52501	86.95235
	$\overline{E}_A^{Sn-Sn}$	2	0.47845	7.69131E-15	3.425971E-13
	$\overline{E}_B$Sn-Sn	2	0.67658	9.63452E-15	1.843157E-13

TABLE 9 Proportional contributions to strengthening.

Alloys	Grain refinement strengthening/ %	Second-phase strengthening/ %	Texture strengthening/ %
Mg-0.5Sn	61.18	14.55	24.27
Mg-2Sn	59.49	17.25	23.26
Mg-4Sn	58.79	21.15	20.06
Mg-6Sn	45.32	22.95	31.73
Mg-8Sn	45.89	23.02	31.09

2. Low-Sn-content alloys (≤2 wt%) are dominated by basal slip and interfacial decohesion, exhibiting typical dimpled fracture morphology. The medium-Sn-content alloy (4 wt%) optimizes DRX and second-phase distribution, enabling synergistic control of dislocation accumulation and plastic deformation. In contrast, high-Sn-content alloys (≥6 wt%) transition toward quasi-cleavage fracture due to increased Mg_2Sn phases and grain boundary weakening, forming a mixed-mode fracture with coexisting dimples and cleavage planes. The Mg-8Sn alloy attains peak strength (ultimate tensile strength: 236 MPa)

via grain refinement (19 μm) and intense texture (pole density: 12.81).

3. Grain refinement provides the dominant strengthening effect (45%–61%), while texture strengthening becomes significant at high Sn content (~31%). Second-phase strengthening scales with Mg_2Sn volume fraction (14.5%–23%). Valence electron theory confirms the critical role of high-energy Mg-Sn bonds in impeding dislocation motion and enhancing stability.

Data availability statement

The original contributions presented in the study are included in the article/Supplementary Material, further inquiries can be directed to the corresponding author.

Author contributions

TS: Writing – original draft. FY: Writing – review and editing. XN: Writing – review and editing. ZJ: Writing – review and editing.

Funding

The author(s) declare that financial support was received for the research and/or publication of this article. The financial support from the Liaoning Province Natural Science Foundation Project of China (2023-MS-321).

Conflict of interest

The authors declare that the research was conducted in the absence of any commercial or financial relationships that could be construed as a potential conflict of interest.

Generative AI statement

The author(s) declare that no Generative AI was used in the creation of this manuscript.

Publisher's note

References

Bu, F., Yang, Q., Qiu, X., Zheng, T., Zhang, D., Niu, X., et al. (2015). Study on the assemblage of Y and Gd on microstructure and mechanical properties of hot extruded Mg-Al-Zn alloy. *Mater. Sci. Eng. A* 639, 198–207. doi:10.1016/j.msea.2015.05.008

Chuanhao, L, Cao, X., Yang, X., and Wang, Y. (2025). Crystal structure optimization and high-throughput intelligent calculation of young's modulus for Al_2O_3-Cr_2O_3 solid solution [J/OL]. *Refractories* 1-7.

Cui, J., Lina, C., Peng, X., Yang, J., Ren, T., Ma, Q., et al. (2024). Phase transition and atomic competition mechanism of *in-situ* particle reinforced TixAl/Ti5Si3 composite coating prepared by laser cladding Al-xSi-2Nb alloy powder on Ti6Al4V alloy. *Surf. and Coatings Technol.* 478, 130402. doi:10.1016/j.surfcoat.2024.130402

Fu, R., Wan, Y., Xiong, X., Yin, D. d., Liu, M. p., Jiang, B., et al. (2024). Compressive twinning behavior of Mg-Sn alloys containing basal or prismatic Mg_2Sn. *Trans. Nonferrous Metals Soc. China* 34 (9), 2800–2813. doi:10.1016/s1003-6326(24)66577-5

Hall, E. O. (1951). The deformation and ageing of mild steel: III discussion of results. *Proc. Phys. Soc. B* 64, 747–753. doi:10.1088/0370-1301/64/9/303

Hu, B., Lei, Yu, Li, H., Wang, Z., Yu, C., and Kang, G. (2024). Experimental observations on the nonproportional multiaxial ratchetting of cast AZ91 magnesium alloy at room temperature. *Int. J. Min. Metall. Mater.* 31 (5), 1115–1125. doi:10.1007/s12613-024-2827-6

Huang, S., Zhao, Q., Yang, Z., Lin, C., Zhao, Y., and Yu, J. (2023). Strengthening effects of Al element on strength and impact toughness in titanium alloy. *J. Mater. Res. Technol.* 26, 504–516. doi:10.1016/j.jmrt.2023.07.206

Kang, J., Wang, C., Deng, K., Nie, K. b., Bai, Y., and Li, W. j. (2017). Microstructure and mechanical properties of Mg 4Zn-0.5Ca alloy fabricated by the combination of forging, homogenization and extrusion process. *J. Alloys Compd.* 720, 196–206. doi:10.1016/j.jallcom.2017.05.232

Li, H., Xu, W., Zhang, Y., Yang, S., Zhang, L., Liu, B., et al. (2024). Prediction of the thermal conductivity of Mg–Al–La alloys by CALPHAD method. *Int. J. Min. Metall. Mater.* 31 (1), 129–137. doi:10.1007/s12613-023-2759-6

Lin, C., Huang, S. X., Yin, G. L., and Zhao, Y. Q. (2016). Development status and prospect of empirical electron theory of solids and molecules. *Ordnance Material Sci. Eng.* 39, 12–28. doi:10.14024/j.cnki.1004-244x.20151228.001

Lin, C., Yin, G., and Zhao, Y. (2015). Calculation of the lattice constant of solids with the use of valence electron structure parameters. *Science* 97, 86–93. doi:10.1016/j.commatsci.2014.10.008

Liu, B., Wei, J., Zhang, S., Zhang, Y., Wu, P., Fang, D., et al. (2024). Microstructures, corrosion behavior and mechanical properties of as-cast Mg–6Zn–2X(Fe/Cu/Ni) alloys for plugging tool applications. *Int. J. Min. Metall. Mater.* 31 (4), 697–711. doi:10.1007/s12613-023-2775-6

Liu, C. Q., Chen, H. W., Liu, H., Zhao, X., and Nie, J. (2018). Metastable precipitate phases in Mg–9.8 wt%Sn alloy. *Acta Mater.* 144, 590–600. doi:10.1016/j.actamat.2017.10.023

Liu, H., Chen, Y., Tang, Y., Wei, S., and Niu, G. (2007). The microstructure, tensile properties, and creep behavior of as-cast Mg–(1–10)%Sn alloys. *J. Alloys Compd.* 440, 122–126. doi:10.1016/j.jallcom.2006.09.024

Liu, Z. L. (2002). *The valence electron structures and composition design in alloys*. 2nd ed. Changchun: Jilin Science and Technology Publishing House.

Liu, Z. L., Li, Z. L., and Liu, W. D. (2002). *Interface electron structure and interface properties [M]*. Beijing: Science Publishing House.

Liu, Z. L., and Lin, C. (2008). *Statistical values of electronic structure parameters and calculation of mechanical properties of alloys*. Beijing: Metallurgical Industry Press.

Ma, J., Lu, X., Prasad Sah, S., Chen, Q., Zhang, Y., and Wang, F. (2024). Enhancing corrosion resistance of plasma electrolytic oxidation coatings on AM50 Mg alloy by inhibitor containing Ba(NO3)2 solutions. *Int. J. Min. Metall. Mater.* 31, 2048–2061. doi:10.1007/s12613-024-2876-x

Ma, K., Wen, H., Hu, T., Topping, T. D., Isheim, D., Seidman, D. N., et al. (2014). Mechanical behavior and strengthening mechanisms in ultrafine grain precipitation-strengthened aluminum alloy. *Acta Mater.* 62, 141–155. doi:10.1016/j.actamat.2013.09.042

Petch, N. (1953). The cleavage strength of polycrystals. *J. Iron Steel Inst. Lond.* 174 (19), 25–28.

Ren, T., Lin, C., Fei, L, Shi, Y., Ma, Q., Huang, S., et al. (2025). A novel multi-scale strategy to reveal martensitic transition and strengthening mechanism in Ti6Al4V alloy. *J. Mater. Sci. and Technol.* 233, 113–131. doi:10.1016/j.jmst.2025.01.048

Saba, F., Zhang, F., Liu, S., and Liu, T. (2019). Reinforcement size dependence of mechanical properties and strengthening mechanisms in diamond reinforced titanium metal matrix composites. *Compos. Part B Eng.* 167, 7–19. doi:10.1016/j.compositesb.2018.12.014

Shen, Q., Ba, Y., Zhang, P., Song, J., Jiang, B., and Pan, F. (2024). Recent progress in the research on magnesium and magnesium alloy foils: a short review. *Int. J. Min. Metall. Mater.* 31 (5), 842–854. doi:10.1007/s12613-024-2846-3

Shi, Z., Zhang, M., Huang, X., Pan, F. S., and Peng, J. (2019). Research progress of age-hardenable mg-sn-based alloys. *Acta Metall. Sin.* 55 (10), 1231–1242. doi:10.11900/0412.1961.2019.00172

Shixing, H., Qi, Z., Lin, C., Wu, C., Zhao, Y., Jia, W., et al. (2021). Effects of oxygen content on charpy impact properties and crack resistance of α titanium alloys. *Mater. Sci. Eng. A* 818, 141394. doi:10.1016/j.msea.2021.141394

Sun, Y., Weng, K., and Yuan, G. (1999). Effect of Sn on microstructure and mechanical properties of magnesium alloys. *Chin. J. Nonferrous Metals* 9 (1), 55–60.

Wang, C., Kang, J., Deng, K., Nie, K. b., Liang, W., and Li, W. g. (2020). Microstructure and mechanical properties of Mg 4Zn-xGd (x=0, 0.5, 1, 2) alloys. *J. Magnesium Alloys* 8 (2), 441–451. doi:10.1016/j.jma.2019.06.005

Wang, J. Z., He, L. J., Lin, C., and Cang, D. (2008). EET research on the Al-22%Si alloy under the action of electric pulses. *Sci. China Ser. E Technol. Sci.* 51, 1930–1938. doi:10.1007/s11431-008-0100-2

Wei, S. H., Chen, Y. G., Tang, Y. B., Pan, F. S., Peng, J., Wang, J. F., et al. (2008). Compressive creep behavior of As-Cast and aging-treated Mg-5Sn alloys. *Mater. Sci. Eng.* A492 (1/2), 20–23. doi:10.1016/j.msea.2008.02.043

Yakubtsov, I. A., Diak, B. J., Sager, C. A., Bhattacharya, B., MacDonald, W., and Niewczas, M. (2008). Effects of heat treatment on microstructure and tensile deformation of Mg AZ80 alloy at room temperature. *Mater. Sci. Eng. A* 496 (1), 247–255. doi:10.1016/j.msea.2008.05.019

Yang, H., Xie, W., Song, J., Dong, Z., Gao, Y., Jiang, B., et al. (2024). Current progress of research on heat-resistant Mg alloys: a review. *Int. J. Min. Metall. Mater.* 31 (6), 1406–1425. doi:10.1007/s12613-023-2802-7

Yang, Z., Li, J. P., Guo, Y. C., Liu, T., Xia, F., Zeng, Z., et al. (2007). Precipitation process and effect on mechanical properties of Mg-9Gd-3Y-0.6Zn-0.5Zr alloy. *Mater. Sci. Eng. A* 454–455, 274–280. doi:10.1016/j.msea.2006.11.047

Yin, S., Zhang, Z., Liu, X., Le, Q., Lan, Q., Bao, L., et al. (2017). Effects of Zn/Gd ratio on the microstructures and mechanical properties of mg-zn-gd-zr alloys. *Mater. Sci. Eng. A* 695, 135–143. doi:10.1016/j.msea.2017.03.117

Yuan, H., Zhang, Y., and Wang, C. (2025). First-principles molecular dynamics study on the conductive mechanism of MnO in submerged arc welding flux [J/OL]. *Acta Metall. Sin.* 1-13.

Zhai, D., Li, X., and Shen, J. (2024). Mechanism of microarc oxidation on AZ91D Mg alloy induced by β-Mg17Al12 phase. *Int. J. Min. Metall. Mater.* 31 (4), 712–724. doi:10.1007/s12613-023-2752-0

Zhang, A., Zhao, Z., Yin, G., and Lin, C. (2017). A novel model to account for the heterogeneous nucleation mechanism of α-Mg refined with Al4C3 in Mg-Al alloy. *Comput. Mater. Sci.* 140, 61–69. doi:10.1016/j.commatsci.2017.08.032

Zhang, R. L. (1990). *The empirical electron theory of solids and molecules*. Changchun: Jilin Science and Technology Publishing House.

Zhang, S., Song, G., Yong, X, Li, Y, Wang, L., Chen, J., et al. (2014). Application of schmid factor in research on microdeformation mechanism of magnesium alloys. *Precis. Form. Eng.* 6 (6), 1–6+39+161.

Zhou, T. (2024). *Research on differential thermal deformation modification, microstructure control and strengthening-toughening mechanism of mg-sn-based alloys*. Beijing, China: China Academic Journals Electronic Publishing House. doi:10.27206/d.cnki.ggsgu.2024.000043

Zhu, L., Qiu, F., Zou, Q., Han, X., Shu, S. L., Yang, H. Y., et al. (2021). Multiscale design of α-Al, eutectic silicon and Mg2Si phases in Al-Si-Mg alloy manipulated by *in situ* nanosized crystals. *Mater. Sci. Eng. A* 802, 140627. doi:10.1016/j.msea.2020.140627

Zhu, Y., Baocheng, L, and Zhang, Z. (2012). Characteristics of magnesium alloys and research progress in their plastic processing technology. *Hot Work. Technol.* 41 (1), 88–91.